



Two-step devitrification of ultrastable glasses

Cecilia Herrero^{a,1} Camille Scalliet^b , M. D. Ediger^c , and Ludovic Berthier^{a,d,1}

Edited by Pablo Debenedetti, Princeton University, Princeton, NJ; received December 7, 2022; accepted March 11, 2023

The discovery of ultrastable glasses raises novel challenges about glassy systems. Recent experiments studied the macroscopic devitrification of ultrastable glasses into liquids upon heating but lacked microscopic resolution. We use molecular dynamics simulations to analyze the kinetics of this transformation. In the most stable systems, devitrification occurs after a very large time, but the liquid emerges in two steps. At short times, we observe the rare nucleation and slow growth of isolated droplets containing a liquid maintained under pressure by the rigidity of the surrounding glass. At large times, pressure is released after the droplets coalesce into large domains, which accelerates devitrification. This two-step process produces pronounced deviations from the classical Avrami kinetics and explains the emergence of a giant lengthscale characterizing the devitrification of bulk ultrastable glasses. Our study elucidates the nonequilibrium kinetics of glasses following a large temperature jump, which differs from both equilibrium relaxation and aging dynamics, and will guide future experimental studies.

glass | supercooled liquid | devitrification | computational methods

Glasses play a critical role in modern technology in applications as diverse as optical fibers and organic light-emitting diode (OLED) displays (1, 2). However, in spite of their solid-like appearance, all glasses spontaneously evolve in a process known as physical aging (3). Aging is an inherent feature of the glassy state that results from its nonequilibrium nature. It is an important challenge because the resulting structural evolution can negatively influence material properties. As a result of recent progress, aging is reasonably well understood if the temperature is lowered by only a few Kelvins near equilibrium. In this case, knowledge of equilibrium response functions allows predictions for the aging dynamics (4). Larger jumps to low temperature are more challenging, but their qualitative features are also well understood (3–7).

By contrast, the opposite case of a large positive temperature jump is much less understood, and enhanced understanding could provide important conceptual advances regarding amorphous materials. Qualitatively different phenomena are observed in comparison to the down jumps and near-equilibrium jumps, with structural relaxation at first occurring very slowly and then accelerating (3, 8). The recent development of ultrastable glasses, accessed via new experimental (9–11) and simulation (12–14) techniques, provides new tools to understand large up-jump experiments. Because these materials are prepared in low-energy states with high kinetic barriers, extreme up-jump experiments can now be performed with a wide variety of experimental techniques.

In the last decade, positive temperature jumps performed from ultrastable states have revealed previously hidden features of amorphous materials. For ultrastable films, the devitrification from the glass to the liquid occurs heterogeneously, starting from the free surface and propagating toward the interior over large distances (>1 micron). This process has been studied extensively in experimental (15–19) and theoretical (20–24) work.

By comparison, fewer studies have investigated the homogeneous devitrification of ultrastable glasses in the bulk (25–28). Surprisingly, macroscopic measurements are best interpreted using an analogy with the nucleation and growth kinetics traditionally observed across first-order phase transitions (15, 29). However, quantitative analysis requires a number of assumptions (15, 28) regarding the underlying physics, which have not independently been tested. Previous simulations used relatively small systems (30, 31) or simplified models (23, 29, 32). Therefore, an understanding of microscopic processes, the characteristic time scales and length scales, and their evolution with glass stability is lacking. At the fundamental level, confirming a deep analogy between crystal melting and devitrification could provide experimental evidence regarding a thermodynamic interpretation of the glass transition (1, 29).

We report results from molecular dynamics simulations which paint a complete microscopic description of the transformation kinetics of ultrastable glasses following a positive temperature jump. We prepare ultrastable configurations at very low initial

Significance

Glassy materials are out-of-equilibrium materials whose properties evolve over long periods of time. Understanding how equilibrium is achieved is an important challenge, particularly for ultrastable glasses and liquids with high kinetic stability. Here, we obtain molecular insights into the equilibration process when temperature is rapidly increased from an ultrastable supercooled liquid. Our simulations show a close analogy between devitrification and crystal melting, with important consequences for understanding the glass transition. Surprisingly, we observe that devitrification is a two-step process, consisting in nucleated liquid droplets that first grow very slowly at the expense of the stiff amorphous matrix. As time advances, the droplets merge into fronts that grow faster. These findings have important consequences for extracting characteristic lengthscales from experimental data.

Author contributions: C.H., C.S., M.D.E., and L.B. designed research; performed research; contributed new reagents/analytic tools; analyzed data; and wrote the paper.

The authors declare no competing interest.

This article is a PNAS Direct Submission.

Copyright © 2023 the Author(s). Published by PNAS. This article is distributed under Creative Commons Attribution-NonCommercial-NoDerivatives License 4.0 (CC BY-NC-ND).

¹To whom correspondence may be addressed. Email: cecilia.herrero-guillen@umontpellier.fr or ludovic.berthier@umontpellier.fr.

This article contains supporting information online at <http://www.pnas.org/lookup/suppl/doi:10.1073/pnas.2220824120/-DCSupplemental>.

Published April 11, 2023.

temperature T_i using the swap Monte Carlo algorithm (13, 33). We instantaneously heat the system to the annealing temperature $T_a > T_i$ and directly observe and quantify how the system devitrifies from its initial low-enthalphy state to the equilibrium liquid at T_a . Generally, our results support and confirm a nucleation and growth kinetics, but they also deviate from the classical Avrami description (34) and from existing interpretations on several aspects. In particular, the liquid droplets that nucleate at short times grow much more slowly than the large domains found at larger times because they contain a liquid that is compressed by the surrounding solid glass matrix. As a result, the large length scale characterizing the bulk devitrification of ultrastable glasses is a physical quantity distinct from the cross-over length scale discussed before for thin films.

We perform molecular dynamics (MD) simulations of a two-dimensional size-polydisperse mixture of $N = 64,000$ soft repulsive particles, known to be a reliable glass-former (35). We prepare ultrastable configurations at number density $\rho_i = 1$, temperature $T_i = 0.035$, and pressure $P_i = 2.31$ using the swap Monte Carlo algorithm (13, 33) and reduced numerical units. We then perform classical MD simulations in the NPT ensemble at pressure P_i for a broad range of annealing temperatures $T_a > T_i$. More information about the model, simulations, and reduced units are provided in *Materials and Methods*.

Results and Discussion

We start in Fig. 1A with a global description of the transformation process for the particular case $T_a = 0.11$. To visualize the transformed regions, we introduce a local structural correlation function $C_B^i(t)$ which records the fraction of nearest neighbors

lost by particle i since $t = 0$ (36). Below, we count a particle as “liquid” whenever $C_B^i(t) \leq 0.5$, but we checked equivalence with several other definitions. We observe that devitrification starts from rare regions distributed throughout the system. As time increases, the size of these regions grows and new regions keep appearing. These observations are broadly consistent with nucleation and growth, but this is distinct from the picture of nuclei preexisting at time $t = 0$ proposed recently (28). At larger times, the growing droplets coalesce and then percolate throughout the system. At very late times, a few glass regions survive, which are eventually invaded by the surrounding liquid. We define the characteristic times t_{tr} and $t_{1/2}$ when, respectively, 99% and 50% of the particles have become liquid.

The time evolution of the density is shown in Fig. 1B for several annealing temperatures T_a . By construction, all curves start from the initial density $\rho_i = 1$, state (I). As a result of the temperature jump from T_i to T_a , the system quickly expands without structural rearrangement to reach the glass state (G) shown in Fig. 1B. Its density is smaller than the initial liquid, $\rho_G < \rho_i$. At much larger times, the glass transforms into the final liquid (L) which has an even lower density, $\rho_L < \rho_G$. Both ρ_G and ρ_L depend on T_a . As found in smaller temperature jumps (3, 8), the dynamics is initially very slow but the glass transformation suddenly accelerates and takes place abruptly. The transformation time t_{tr} increases by 5 orders of magnitude with decreasing the annealing temperature T_a , Fig. 1B.

The transformation kinetics can be quantified using the fraction $x_l(t)$ of liquid particles at time t , which goes from 0 at $t = 0$ to 1 at long times; Fig. 1C. To compare different T_a , we rescale the time axis by t_{tr} as defined above. As T_a decreases, the time evolution of $x_l(t)$ becomes much sharper and

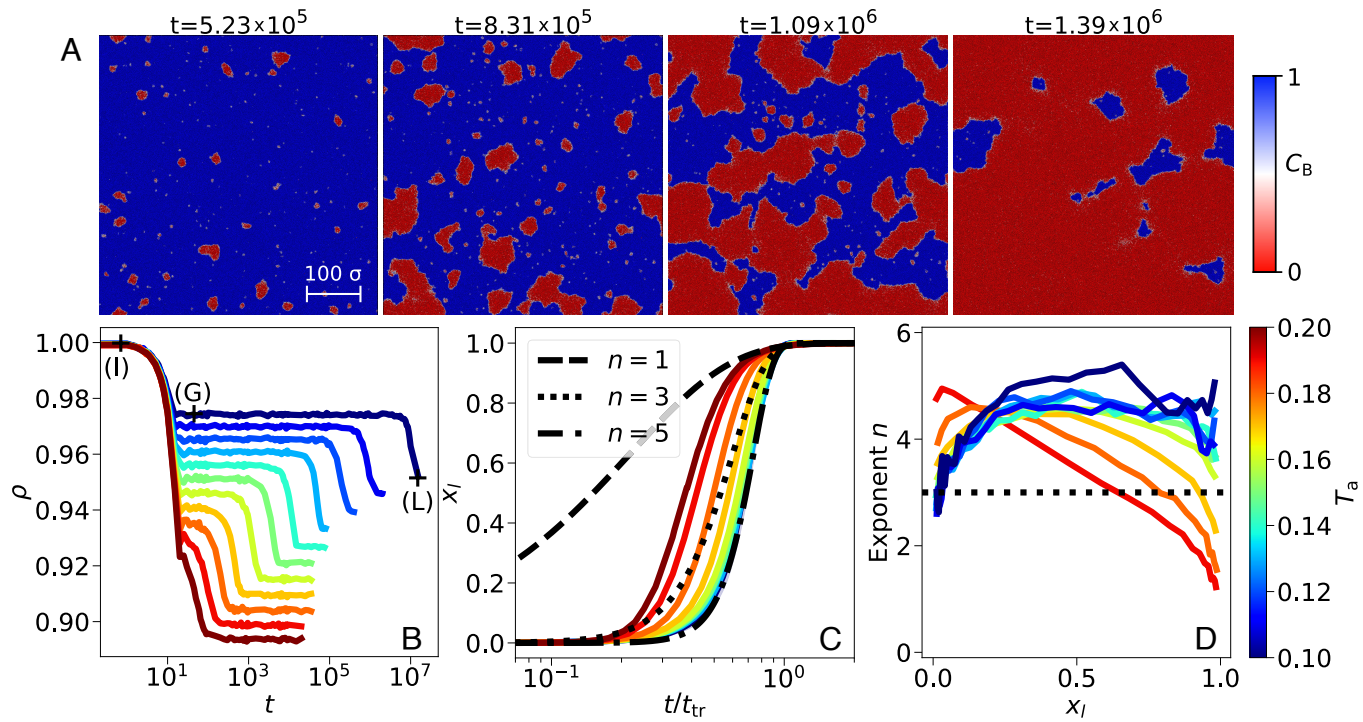


Fig. 1. Transformation of an ultrastable glass into an equilibrium liquid. (A) Visualizing the transformation of an ultrastable glass prepared at $T_i = 0.035$ annealed at $T_a = 0.11$ with $N = 256000$ at times t indicated on the figure. The bond-breaking correlation distinguishes the glass with $C_B^i = 1$ (blue) from the liquid with $C_B^i = 0$ (red). Rare isolated liquid droplets nucleate, grow slowly, and then coalesce to transform the entire system. (B) Time evolution of number density ρ for $T_i = 0.035$ and different annealing temperatures T_a . The initial glass (I) rapidly expands to the glass state (G), and transforms over a much slower time scale into the equilibrium liquid (L). (C) Time evolution of the liquid fraction $x_l(t)$ for the same parameters as (B). The time axis is normalized by the transformation time t_{tr} . Dashed lines: Avrami functions $1 - \exp(-Kt^n)$ with different exponents n . (D) Evolution of the effective exponent n as a function of $x_l(t)$. The dashed classical Avrami value $n = 3$ does not adequately describe our results.

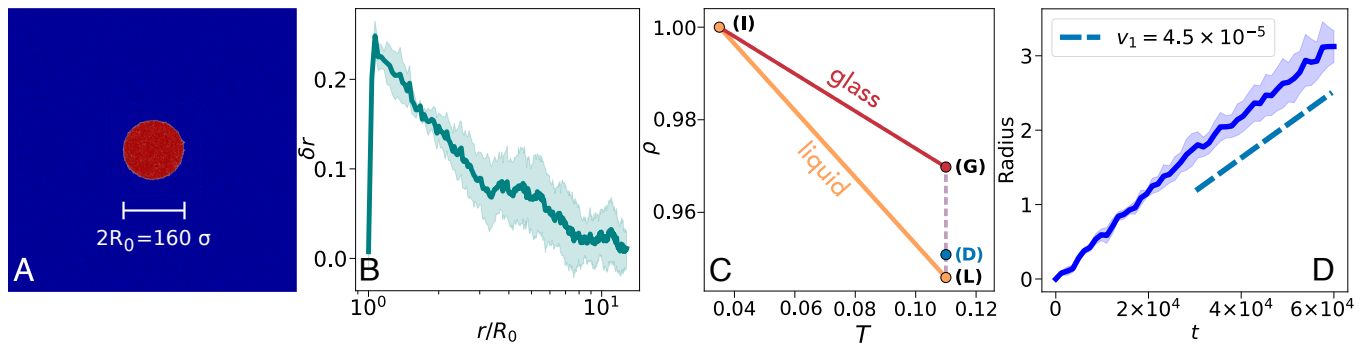


Fig. 2. Understanding the early stages of the transformation by simulating isolated droplets. (A) Snapshot of a single liquid droplet of radius $R_0 = 80$ in a large $N = 576000$ sample. Color code provided in Fig. 1A. (B) Radial displacement field in the glass after mechanical equilibrium is reached for $R_0 = 30$. (C) Liquid and glass equations of state showing the initial state (I), the expanded glass (G), and final liquid (L) for $T_i = 0.035$ and $T_a = 0.11$. (D) The time evolution of the droplet radius allows us to measure the growth velocity v_1 of isolated droplets containing the compressed liquid.

eventually collapses onto a master curve for the lowest annealing temperatures studied.

Following previous studies (15, 23, 28), we fit $x_l(t)$ to a generic Avrami expression (34)

$$x_l(t) = 1 - \exp(-Kt^n). \quad [1]$$

In the classical Avrami picture, a nucleation rate describes the initiation of droplets, and a constant velocity captures their growth. Both parameters then enter the definition of the constant K in Eq. 1, and the exponent is predicted to be $n = d + 1$, with d the spatial dimension. The classical Avrami prediction would thus be $n = 3$ for our two-dimensional simulations. We show in Fig. 1C that this classic exponent does not describe our measurements accurately. To better quantify these deviations, we follow the experimental literature and report the parametric evolution of the effective exponent n as a function of x_l in Fig. 1D, using time as an implicit variable. While n is not well defined at high T_a , it consistently takes a surprisingly large value $n \approx 4.5$ for low T_a , indicating a breakdown of the classical nucleation and growth picture. In the following, we deploy original numerical strategies to quantitatively account for the observed behavior.

In the early stages of the transformation, Fig. 1A demonstrates that the system is composed of isolated liquid droplets confined by the surrounding glass matrix. To better understand this situation and characterize the state of the system, we have analyzed an idealized version of this geometry with a single liquid droplet of radius $R_0 \gg 1$ immersed in a very large glass matrix of linear size $L \gg R_0$, Fig. 2A. We used $L \approx 770$ and found identical results for $R_0 = 30, 50, 80$, and 100 . Therefore, the results presented for this geometry are intrinsic, in the sense that they do not depend on the system or droplet sizes, or the employed numerical strategy, and genuinely reflect the behavior of an isolated liquid droplet in the stable glass matrix. Our protocol, detailed in *Materials and Methods*, is the following. We start from the glassy state (G) in Fig. 1B and perform high-temperature dynamics in a spherical domain of radius R_0 to transform this region, followed by thermalization at T_a . This is done while keeping the particles outside the cavity immobile. At this stage, the density in the liquid droplet is thus equal to that of the glass (G), implying that the liquid pressure has increased above P_i . Then, we simulate the dynamics of the whole sample at temperature T_a and constant volume. At the very beginning of the simulation, the compressed liquid exerts pressure on the surrounding glassy particles to expand, but the expansion is opposed by the rigidity of the glass, until a mechanical equilibrium is found. We have computed the radial displacement in the glass right after mechanical equilibrium

is reached. Its angular-averaged amplitude δr , shown in Fig. 2B, is maximal at the edge of the droplet $r/R_0 = 1$ and decays algebraically to zero at large distances. Consequently, the droplet expands from R_0 to $R_0 + \Delta R$ so that its density decreases by $\Delta\rho \approx 2\rho_G\Delta R/R_0$. The corresponding droplet (D) density $\rho_D = \rho_G - \Delta\rho$ is shown in Fig. 2C together with the other state points. Far from the droplet, the glass pressure is equal to P_i , as it should be. The pressure is however larger in the droplet which contains a liquid at density ρ_D and pressure $P_D > P_i$ and thus distinct from the final equilibrium liquid (L) at conditions (P_i, T_a) . The pressure difference between the coexisting liquid droplet and the surrounding solid is expected and results from both the surface tension between the two phases and the surface stress that exists generically at solid–liquid interfaces (37, 38).

At much longer times, structural relaxation occurs and the liquid droplet grows slowly. We monitor the time evolution of the liquid fraction $x_l(t)$, which is directly connected to the growing radius $R(t)$ since $x_l(t) \propto R^2(t)$. In Fig. 2D, we show that the droplet size increases linearly with time, $R(t) = R_0 + v_1 t$, with a velocity v_1 that can be measured numerically. We have confirmed that the same value v_1 describes the growth of isolated droplets randomly selected in the real process illustrated in Fig. 1. This demonstrates that the idealized geometry with a single droplet depicted in Fig. 2 faithfully represents the initial stages of the bulk devitrification.

To better characterize the late times at which very large liquid domains percolate throughout the system, we again introduce an idealized geometry, as shown in Fig. 3A, where we create a single

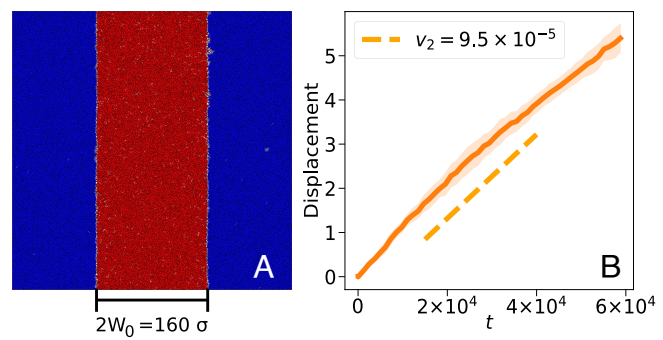


Fig. 3. Understanding the late stages of the transformation by simulating a macroscopic interface. (A) Snapshot of a two-front system with $N = 64,000$. Color code as in Fig. 1A. (B) The time evolution of the interface position allows us to measure the growth velocity v_2 of large fronts.

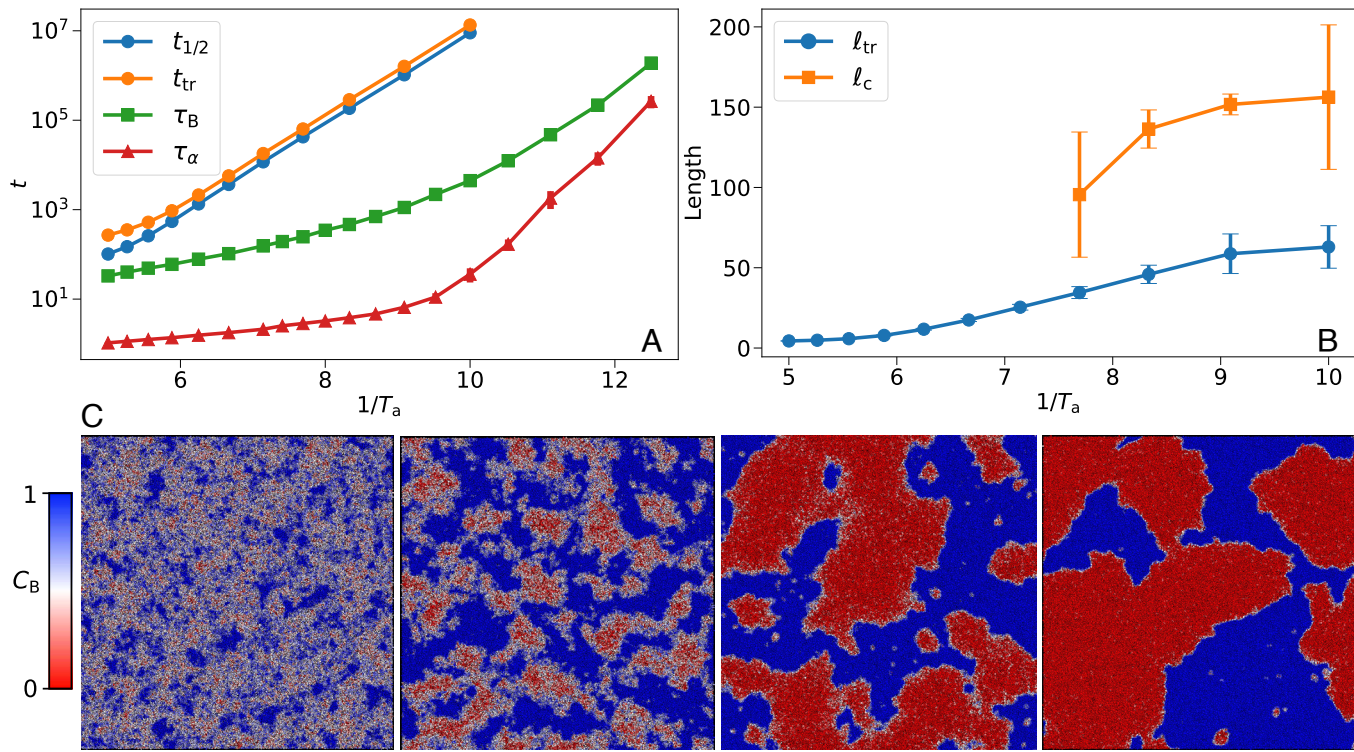


Fig. 4. Characteristic time scales and length scales of ultrastable glass transformation. (A) Temperature dependence of the transformation time t_{tr} and two characteristic times of the equilibrium liquid: τ_B defined from C_B and τ_α from $F_2(q, t)$. (B) Characteristic lengths of the process: ℓ_{tr} is the characteristic size of the domains at time $t_{1/2}$ and the cross-over length $\ell_c = v_2 t_{\text{tr}}$. (C) Snapshots taken at time $t_{1/2}$ for $N = 64,000$ and different annealing temperatures $T_a = 0.20, 0.17, 0.13, 0.10$ (from Left to Right).

percolating liquid domain (30) of width $2W_0$. The numerical strategy is similar to that for the droplet geometry; *Materials and Methods*. Once the vertical liquid domain is prepared, we run *NPT* simulations at temperature T_a and pressure P_i for the whole sample. In this case, the pressure is homogeneous across the system and the liquid density is ρ_L . As time increases, we observe that the liquid propagates toward the glass as a front. We extract its velocity by monitoring the time evolution of $x_l(t)$, which is directly proportional to the displacement of the interface. This is shown in Fig. 3B for $T_a = 0.11$. The front propagation is again ballistic, with $x_l(t) \propto v_2 t$ which defines the front velocity v_2 . Again, we have checked that the same value v_2 describes the growth of large interfaces randomly selected in the real transformation process shown in Fig. 1, confirming the relevance of the idealized geometry studied in Fig. 3.

By gathering velocity measurements for different annealing temperatures and the two idealized geometries shown in Figs. 2 and 3 we find that the growth of large interfaces is systematically faster than the growth of isolated droplets, $v_1 < v_2$. This is because the liquid inside droplets is under pressure $P_D > P_i$ and its relaxation time is thus larger than the one of the equilibrium liquid (L). For a given T_i , we observe that the velocity difference $v_2 - v_1$ increases with increasing T_a , because the separation between the points (G) and (L) increases in Fig. 2C. For a given T_a , we also find a larger difference in the velocities for lower T_i because the glass becomes stiffer and it can resist better the expansion of the liquid droplet at short times.

The quantitative comparison between the kinetics of isolated droplets and large fronts demonstrates that a central assumption leading to Avrami kinetics does not hold for the bulk devitrification of ultrastable glasses as there is not a unique velocity describing the entire process. This feature is unique

to the systems we study because a small pressure difference in the supercooled liquid typically translates into a large difference in the relaxation times (3). We argue that this more complex two-step process is responsible for the anomalously large value of the exponent n shown in Fig. 1E. First, we note that at early times $x_l \ll 1$ when only isolated droplets exist, the classical value $n = 3$ is observed. However, as the liquid fraction grows and droplets start to coalesce, n grows to a much larger value $n \approx 4.5$. Qualitatively, this implies that the transformation process accelerates further, as expected if the velocity increases from v_1 to v_2 . In *SI Appendix*, we show that adding the simplest hypothesis of a smooth transition between two velocities v_1 and $v_2 > v_1$ in the analytic Avrami description generically produces values $n \approx 5$, which supports our physical interpretation of the numerical results. Note that the pressure effect, which controls kinetic stability and the devitrification melting, is absent in several simulation studies (23, 29, 30, 32).

Finally, we collect in Fig. 4 the relevant time scales and length scales characterizing the devitrification of ultrastable glasses. Starting with times in Fig. 4A, the slowest time scale is the transformation time t_{tr} , which is much larger than any time scale characterizing the equilibrium relaxation of the liquid in the same conditions. We display the decay time of the bond-breaking correlation $C_B(t)$, τ_B , and of the self-intermediate scattering function, τ_α , defined in the *Materials and Methods*. The kinetic stability encoded in the ratio between t_{tr} and these equilibrium relaxations reaches a large value 10^3 to 10^5 at the lowest T_a and would increase further if longer timescales could be simulated allowing access to even lower T_a . This large kinetic stability is comparable to values previously reported in both vapor deposited films (17, 19, 39) and computer glasses generated with the particle-swap algorithm (24, 31).

Turning to length scales, we report in Fig. 4*B* the evolution of the characteristic transformation length ℓ_{tr} suggested by Fig. 4*C* where snapshots of the system at various annealing temperatures T_a are shown at time $t_{1/2}$ when half of the glass has transformed. These images reveal that the transformation process is highly heterogeneous in space, with a characteristic length scale ℓ_{tr} which grows as kinetic stability increases. To characterize this length, we employ a method described in detail in the Methods section based on the determination of the chord length distributions, following the same recipe as in refs. 40 and 41. Briefly, we transform the particle configuration into a coarse-grained binary lattice of glass and liquid cells and measure the length of horizontal and vertical segments (or “chords”) which intersect the liquid (red) domains. We define ℓ_{tr} , the average linear size of liquid domains, as the first moment of the chord distribution. As shown in Fig. 4*B*, ℓ_{tr} grows with decreasing T_a reaching $\ell_{\text{tr}} \approx 60$ for $T_a = 0.10$ and a kinetic stability of about 4×10^5 . In these conditions, the transformed domains barely fit in our simulation box of linear size $L \approx 250$; *Rightmost* snapshot in Fig. 4*C*.

In experimental studies of thin films transforming via front propagation, a large “cross-over” length scale ℓ_c has been reported (15, 19). It is defined as the distance traveled by the liquid front over the transformation time of the corresponding bulk system. Using our notations, we can express it as $\ell_c = v_2 t_{\text{tr}}$, and it can be determined from our independent measurements of v_2 and t_{tr} . Previous work (15, 19, 28) assumed that the two length scales ℓ_{tr} and ℓ_c are equal. This is indeed correct when the classical Avrami picture applies (29). Our results however imply that this picture does not describe the transformation of ultrastable glasses. In Fig. 4*B*, we confirm that while the two characteristic length scales are both large, they are distinct and evolve differently with T_a . Again, the existence of two distinct velocities rationalizes this finding. A smaller value $v_1 < v_2$ in the first stages of devitrification implies that t_{tr} and, thus, ℓ_c are larger than if $v_1 = v_2$. Instead, a longer t_{tr} allows more time for droplets to nucleate so that ℓ_{tr} , which is controlled by the typical distance between droplets, decreases. The opposite influence of the velocity contrast v_2/v_1 on physical length scales implies that, in general, ℓ_{tr} is distinct from, and smaller than, ℓ_c .

Conclusions

We offer a computational study of the devitrification of ultrastable glasses which reveals several unexpected results that had not been predicted by previous theoretical models and have either not been observed experimentally or contradict published results. We now discuss these important points.

Our first observation is the nucleation at short times of liquid droplets containing a liquid that is under pressure. This finding stems from the large density difference between the ultrastable glass and the equilibrium liquid, combined with the rigidity of the surrounding glass; Fig. 2. Such a pressure difference is generically expected for any solid–liquid transformation (37). Although these two effects may quantitatively differ in different materials, it is difficult to imagine a physical relaxation process that would entirely release this pressure. This finding has several important consequences. First, it implies that the liquid that first appears during the transformation has a relaxation dynamics that is much slower than the equilibrium liquid that forms at long times. Published works probing these dynamics have not reported any evidence for such a slow process (17, 27, 28), and future experiments should revisit this point. A related consequence is that the growth of these compressed liquid droplets is much

slower than the growth of the fronts propagating from a free surface. This directly contradicts an important assumption made in refs. 15 and 28 to interpret experimental results. To our knowledge, the growth of isolated droplets has not yet been studied experimentally.

A final consequence is that the growth velocity of the liquid phase is not a constant during the transformation, which directly explains the emergence of an anomalously large Avrami exponent describing the transformation kinetics. This finding constitutes our second key observation. It contrasts with the recent report of a smaller exponent extracted from calorimetric measurements (28). These recent results were explained by hypothesizing a population of liquid droplets preexisting at time $t = 0$ and initiating the transformation without invoking time-distributed nucleation events. This description is in contrast with our simulations, where the appearance of new liquid droplets is instead slow and randomly distributed in time. We can invoke only two important differences between simulations and experiments that could explain this discrepancy. We directly determine the liquid fraction $x_l(t)$ *in situ*, whereas in experiments, it is indirectly inferred from calorimetric measurements involving a complicated thermal treatment and data analysis. Another difference is the devitrification time window analyzed in simulations, which is of order 10 ms in simulations, but about 10^3 times slower in most experiments (28).

Our third key observation is that a large length scale characterizes the transformation process, which becomes larger as the kinetic stability of the glass increases. Despite our numerical constraints, we directly measure a length scale approaching $\ell_{\text{tr}} \approx 100\sigma$ which would presumably grow larger if we could simulate longer time scales. We are not aware of any bulk relaxation process in equilibrium supercooled liquids of simple glass-formers that can reach such large values, although experiments have reported variation of glass temperatures compatible with large characteristic lengths in polymeric systems (~ 100 to 200 nm) (42, 43). Qualitatively, the large length scale ℓ_{tr} reflects the equally large distance between nucleated liquid droplets in the early stages of the transformation. As T_a decreases, droplets become more sparse as their nucleation rate decreases, and ℓ_{tr} increases. Therefore, it is the large barrier to nucleating liquid droplets which is responsible for the emergence of a large length scale. This interpretation explains why such large length scales have never been found in conventional glasses as these less stable systems would have smaller barriers.

There has been extensive experimental work deducing that a large cross-over length scale ℓ_c appears in thin film transformation via the propagation of a front. We have shown that these two length scales are conceptually and quantitatively distinct. In particular, ℓ_c simply represents a cross-over between distinct physical regimes during front propagation but does not characterize any kind of spatial correlations, contrary to ℓ_{tr} . The length scale ℓ_{tr} has recently been indirectly inferred from experiments, but this assumes hypotheses which do not hold in our simulations. A more direct experimental measurement of the large length scale ℓ_{tr} is an important target for future work. Because of the density difference between transformed and untransformed regions, this could in principle be achieved with small-angle X-ray scattering experiments.

More fundamentally, the observation that the transformation of an ultrastable glass into a liquid proceeds via a physical mechanism traditionally observed for first-order transitions raises important questions. It was argued in ref. 29 that the existence of a thermodynamic Kauzmann transition would indeed provide

the needed ingredients to interpret this analogy. In the alternative approach of ref. 23 based on a kinetically constrained model, the additional introduction of some thermally activated nucleation sites was also needed to reproduce the observed phenomenology, with the growth processes controlled by dynamic facilitation. Future work should therefore concentrate on the first stages of the transformation to understand better their physical origin in order to reach a level of understanding for nucleation from glasses similar to the detailed knowledge gained for crystals (44, 45). It would also be very interesting to understand whether the regions that first transform are related to specific structural features of ultrastable glassy states.

Note added: Experimental work that appeared after our work was submitted (46) shows real-space images of a transforming thin film of an ultrastable glass. This new study shows several features consistent with our simulations: a characteristic length scale on the order of 1 micron, continuous nucleation of new transformation sites, and indications of large Avrami exponents.

Supporting Information Appendix (SI). *SI Appendix* provides a description of the theoretical framework for classical and anomalous Avrami exponent for nonconstant growth velocity, Monte Carlo simulations of Avrami kinetics and nonconstant velocity, a discussion on the influence of the kinetics on the transformation length, and supporting figures.

Materials and Methods

Size-Polydisperse Model Glass-Former. We perform molecular dynamics (MD) simulations of a two-dimensional size-polydisperse mixture, which is well characterized (35). The system is composed of soft repulsive spheres whose diameters σ_i follow the probability distribution $\mathcal{P}(\sigma_i) = A\sigma_i^{-3}$, with A a normalization constant, $\sigma_i \in [\sigma_{\min}, \sigma_{\max}]$, $\sigma_{\min}/\sigma_{\max} = 0.45$, and $\sigma_{\max} = 1.62$. The pair interaction potential is given by

$$V_{ij}(r) = \varepsilon \left(\frac{\sigma_{ij}}{r} \right)^{12} + c_0 + c_2 \left(\frac{r}{\sigma_{ij}} \right)^2 + c_4 \left(\frac{r}{\sigma_{ij}} \right)^4; \quad [2]$$

where $r = |\mathbf{r}_i - \mathbf{r}_j|$ (\mathbf{r}_i being the position of particle i), and nonadditive interactions $\sigma_{ij} = 0.5(\sigma_i + \sigma_j)(1 - 0.2|\sigma_i - \sigma_j|)$. We use reduced units based on the particle mass m , the energy scale ε , and a microscopic length σ defined as the average particle diameter. The time unit is $\tau_{\text{LJ}} = \sigma\sqrt{m/\varepsilon}$. The parameters $c_0 = -28\varepsilon/r_c^{12}$, $c_2 = 48\varepsilon/r_c^{14}$, and $c_4 = -21\varepsilon/r_c^{16}$ ensure that the potential V_{ij} is continuous up to its second derivative at the cutoff distance $r_c = 1.25\sigma_j$.

Simulating the Transformation of an Ultrastable Glass into a Liquid. The initial configuration is composed of $N = 64,000$ particles at a number density $\rho_i = N/L^2 = 1$, in a square box of linear size L and periodic boundary conditions. The initial state is equilibrated using the swap Monte Carlo algorithm (33), at a temperature $T_i = 0.035 \approx T_g/2$, with T_g the experimental glass transition temperature. The corresponding pressure is $P_i = 2.31$. The MD simulations are performed using a Nosé-Hoover thermostat at temperatures $T_a \in [0.1, 0.2]$ and a barostat at pressure P_j . The discretization timestep is set to 0.01. For each T_a , we perform MD simulations starting from 8 initial independent configurations, with 3 different sets of initial velocities, therefore gathering statistics for 24 different runs per T_a . The error bars were computed from the statistical error within 95% of the confidence level. In order to test for possible finite size effects, we performed equivalent MD simulations for a system composed of $N = 2,56,000$ particles, running 3 different configurations for $T_a = 0.11, 0.12$, and 0.13 and obtained equivalent results.

Simulations of Isolated Droplets. The key technical aspect of these simulations is to allow the system to relax mechanically and possess an inhomogeneous

pressure profile. We have found that the following strategy satisfies our needs. We start from the same initial configurations as in the full phase-transformation simulations using an *NPT* simulation at $T = T_a$ and P_j . The expanded glass (G) is reached after a short time, shown in Fig. 2A. Immediately after this rapid expansion, we replicate the system three times in both dimensions, resulting in a glass with $N = 5,76,000$ particles with pressure P_j . Such a large system size is needed to ensure that the mechanical response of the glass matrix is not affected by finite size effects or, equivalently, to ensure that the liquid droplet does not interact mechanically with its replicated images. We insert a liquid droplet in this large glass matrix by performing high-temperature dynamics, at $T = 0.8$ during $10^2 \tau_{\text{LJ}}$ in a circular cavity of radius R_0 , keeping all other particles fixed. This is followed by additional simulations inside the cavity at temperature T_a for $10^4 \tau_{\text{LJ}}$ to ensure equilibration inside the cavity. We then perform *NVT* simulations of the entire system at T_a . In the first stages of these simulations, the liquid droplet expands into the glass matrix, which pushes back until mechanical equilibrium is reached, state (D) in Fig. 3C. In this state, we have measured the pressure P_D inside the droplet using different methods. First, we used direct computation from the diagonal components of the pressure tensor in a large portion of the liquid droplet. We confirmed that the potential energy and structural relaxation time correspond to the pressure P_D . We also measured the expansion of the droplet by following the displacement field in the radial direction. The resulting density ρ_D agrees with the measured pressure P_D . At a given T_a , simulations were performed for three different droplet sizes $R_0 = 50, 80$, and 100 , which gave identical results. We also checked that our results do not depend on the specific initial configuration.

Simulations of Macroscopic Fronts. For large fronts, we again start from the expanded glass state (G), but we do not need to replicate the system in both directions. We directly perform high-temperature simulations to transform a slit of width $2W_0$ into a liquid, as shown in Fig. 3A. This is followed by some dynamics at T_a . We then perform *NPT* simulations at pressure P_j and temperature T_a . At a given T_a , simulations were performed for three different widths $W_0 = 50, 80$, and 100 . We also checked that our results do not depend on the specific initial configuration.

Bond-Breaking Correlation Function and Phase Definition. We distinguish between the glass and liquid states using the bond-breaking correlation function given by

$$C_B^i(t) = \frac{n_i(t|0)}{n_i(0)}, \quad [3]$$

where $n_i(t)$ is the number of neighbors of particle i at time t and $n_i(t|0)$ is the number of neighbors of particle i at time t that were also neighbor at $t = 0$. At $t = 0$, the neighbors of particle i are defined as all particles $j \neq i$ whose interparticle distance is smaller than a threshold, $r_{ij}/\sigma_{ij} < 1.35$, which corresponds to the first minima of the rescaled radial distribution function $g(r/\sigma_{ij})$. We define liquid particles as those with $C_B^i(t) \leq 0.5$. The bond-breaking correlation function is defined from the ensemble average:

$$C_B(t) = \left\langle \frac{1}{N} \sum_{i=1}^N C_B^i(t) \right\rangle, \quad [4]$$

where N is the number of particles. One can define from the bond-breaking correlation a characteristic time for the structural relaxation of the equilibrium bulk system as $C_B(t = \tau_B) = 0.5$.

Self-Intermediate Scattering Function. We use another common correlation function to characterize the bulk dynamics, namely the self-intermediate scattering function, given by

$$F_S(t) = \left\langle \frac{1}{N} \sum_{i=1}^N \cos[\mathbf{q} \cdot \delta \mathbf{r}_i(t)] \right\rangle, \quad [5]$$

where $\delta \mathbf{r}_i = \mathbf{r}_i(t) - \mathbf{r}_i(0)$ and wave vectors with $|\mathbf{q}| = 6.9$, corresponding to the position of the global maximum in the static structure factor $S(\mathbf{q})$. We define the α -relaxation time as $F_S(t = \tau_\alpha) = 1/e$. For large 2d systems, $F_S(t)$

can be affected by Mermin–Wagner fluctuations, which depend logarithmically on the system size (47). To avoid this effect, we performed bulk MD equilibrium simulations of a relatively small system with $N = 2,000$.

Chord Length Distribution and Characteristic Length Scale. We employ the chord length distribution (40, 41) to characterize the size of the liquid domains. Briefly, we discretize the spatial coordinates on a grid with cells of linear size 1.47 so that the cell is large enough to ensure that there is at least one particle in the cell (36). Then, we average C_B^i over all the particles in a given cell. We binarize the result so that the cell is either in state 0 (liquid) when $C_B^i \leq 0.5$ or 1 (glass) otherwise. The chord length ℓ is then defined from the intersection of segments in the x and y directions with the liquid domains. By averaging over all segments in both directions, we get the chord length distribution $P(\ell)$, and we extract a characteristic length scale as the first moment of this distribution.

Data, Materials, and Software Availability. The ASCII files (examples of input scripts) needed to reproduce all the simulations in the present study have

been deposited in Github (<https://github.com/ceciherr/bulkDevitrification>). Due to the large size, the produced trajectories are available upon reasonable request.

ACKNOWLEDGMENTS. This work was publicly funded through ANR (the French National Research Agency) under the Investissements d’avenir programme with the reference ANR-16-IDEX-0006. It was also supported by a grant from the Simons Foundation (#454933, L.B.) and the European Research Council under the EU’s Horizon 2020 Program, Grant No. 740269 (C.S.), the US NSF, CHE-2153944 (M.D.E.), and by a Visiting Professorship from the Leverhulme Trust (VP1-2019-029, L.B.). C.S. acknowledges support from a Herchel Smith Fellowship, University of Cambridge, and a Ramon Jenkins Research Fellowship from Sidney Sussex College, Cambridge.

Author affiliations: ^aLaboratoire Charles Coulomb (L2C), Université de Montpellier, CNRS, Montpellier 34095, France; ^bDepartment of Applied Mathematics and Theoretical Physics, University of Cambridge, Cambridge CB3 0WA, United Kingdom; ^cDepartment of Chemistry, University of Wisconsin–Madison, Madison, WI 53706; and ^dYusuf Hamied Department of Chemistry, University of Cambridge, Cambridge CB2 1EW, United Kingdom

1. L. Berthier, M. D. Ediger, Facets of glass physics. *Phys. Today* **69**, 40–46 (2016).
2. J. Ràfols-Ribé *et al.*, High-performance organic light-emitting diodes comprising ultrastable glass layers. *Sci. Adv.* **4**, eaar8332 (2018).
3. C. A. Angell, K. L. Ngai, G. B. McKenna, P. F. McMillan, S. W. Martin, Relaxation in glassforming liquids and amorphous solids. *J. Appl. Phys.* **88**, 3113–3157 (2000).
4. B. Riechers *et al.*, Predicting nonlinear physical aging of glasses from equilibrium relaxation via the material time. *Sci. Adv.* **8**, eabl9809 (2022).
5. G. W. Scherer, Theories of relaxation. *J. Non-Crystall. Solids* **123**, 75–89 (1990).
6. I. Hodge, Enthalpy relaxation and recovery in amorphous materials. *J. Non-Crystall. Solids* **169**, 211–266 (1994).
7. S. Simon, J. Y. Park, G. McKenna, Enthalpy recovery of a glass-forming liquid constrained in a nanoporous matrix: Negative pressure effects. *Euro. Phys. J. E* **8**, 209–216 (2002).
8. A. J. Kovacs, “Transition vitreuse dans les polymères amorphes” in *étude phénoménologique in Fortschritte der hochpolymeren-forschung* (Springer, 1964), pp. 394–507.
9. S. F. Swallen *et al.*, Organic glasses with exceptional thermodynamic and kinetic stability. *Science* **315**, 353–356 (2007).
10. M. D. Ediger, Perspective: Highly stable vapor-deposited glasses. *J. Chem. Phys.* **147**, 210901 (2017).
11. C. Rodriguez-Tinoco, M. Gonzalez-Silveira, M. A. Ramos, J. Rodriguez-Viejo, Ultrastable glasses: New perspectives for an old problem. *La Rivista del Nuovo Cimento* **45**, 325–406 (2022).
12. L. Berthier, D. Coslovich, A. Ninarello, M. Ozawa, Equilibrium sampling of hard spheres up to the jamming density and beyond. *Phys. Rev. Lett.* **116**, 238002 (2016).
13. A. Ninarello, L. Berthier, D. Coslovich, Models and algorithms for the next generation of glass transition studies. *Phys. Rev. X* **7**, 021039 (2017).
14. A. D. S. Parmar, M. Ozawa, L. Berthier, Ultrastable metallic glasses in silico. *Phys. Rev. Lett.* **125**, 085505 (2020).
15. K. L. Kearns, M. D. Ediger, H. Huth, C. Schick, One micrometer length scale controls kinetic stability of low-energy glasses. *J. Phys. Chem. Lett.* **1**, 388–392 (2010).
16. D. M. Walters, R. Richert, M. D. Ediger, Thermal stability of vapor-deposited stable glasses of an organic semiconductor. *J. Chem. Phys.* **142**, 134504 (2015).
17. A. Sepúlveda, M. Tylinski, A. Guiseppi-Elie, R. Richert, M. D. Ediger, Role of fragility in the formation of highly stable organic glasses. *Phys. Rev. Lett.* **113**, 045901 (2014).
18. J. Ràfols-Ribé, M. González-Silveira, C. Rodríguez-Tinoco, J. Rodríguez-Viejo, The role of thermodynamic stability in the characteristics of the devitrification front of vapour-deposited glasses of toluene. *Phys. Chem. Chem. Phys.* **19**, 11089–11097 (2017).
19. C. Rodríguez-Tinoco *et al.*, Surface-bulk interplay in vapor-deposited glasses: Crossover length and the origin of front transformation. *Phys. Rev. Lett.* **123**, 155501 (2019).
20. P. G. Wolynes, Spatiotemporal structures in aging and rejuvenating glasses. *Proc. Natl. Acad. Sci. U.S.A.* **106**, 1353–1358 (2009).
21. S. Léonard, P. Harrowell, Macroscopic facilitation of glassy relaxation kinetics: Ultrastable glass films with frontlike thermal response. *J. Chem. Phys.* **133**, 244502 (2010).
22. A. Wisitorsasak, P. G. Wolynes, Dynamical heterogeneity of the glassy state. *J. Phys. Chem. B* **118**, 7835–7847 (2014).
23. R. Gutiérrez, J. P. Garrahan, Front propagation versus bulk relaxation in the annealing dynamics of a kinetically constrained model of ultrastable glasses. *J. Stat. Mech.: Theory Exp.* **2016**, 074005 (2016).
24. E. Flener, L. Berthier, P. Charbonneau, C. J. Fullerton, Front-mediated melting of isotropic ultrastable glasses. *Phys. Rev. Lett.* **123**, 175501 (2019).
25. A. Sepúlveda, S. F. Swallen, M. D. Ediger, Manipulating the properties of stable organic glasses using kinetic facilitation. *J. Chem. Phys.* **138**, 12A517 (2013).
26. C. Rodríguez-Tinoco, J. Ràfols-Ribé, M. González-Silveira, J. Rodríguez-Viejo, Relaxation dynamics of glasses along a wide stability and temperature range. *Sci. Rep.* **6**, 1–8 (2016).
27. J. Ràfols-Ribé *et al.*, Kinetic arrest of front transformation to gain access to the bulk glass transition in ultrathin films of vapour-deposited glasses. *Phys. Chem. Chem. Phys.* **20**, 29989–29995 (2018).
28. A. Vila-Costa *et al.*, Nucleation and growth of the supercooled liquid phase control glass transition in bulk ultrastable glasses. *Phys. Rev. Lett.* **124**, 076002 (2020).
29. R. L. Jack, L. Berthier, The melting of stable glasses is governed by nucleation-and-growth dynamics. *J. Chem. Phys.* **144**, 244506 (2016).
30. G. M. Hocky, L. Berthier, D. R. Reichman, Equilibrium ultrastable glasses produced by random pinning. *J. Chem. Phys.* **141**, 224503. (2014).
31. C. J. Fullerton, L. Berthier, Density controls the kinetic stability of ultrastable glasses. *EPL (Europhys. Lett.)* **119**, 36003 (2017).
32. M. Lulli, C. S. Lee, H. Y. Deng, C. T. Yip, C. H. Lam, Spatial heterogeneities in structural temperature cause Kovacs’ expansion gap paradox in aging of glasses. *Phys. Rev. Lett.* **124**, 095501 (2020).
33. L. Berthier, E. Flener, C. J. Fullerton, C. Scalliet, M. Singh, Efficient swap algorithms for molecular dynamics simulations of equilibrium supercooled liquids. *J. Stat. Mech.: Theory Exp.* **2019**, 064004 (2019).
34. M. Avrami, Kinetics of phase change. I general theory. *J. Chem. Phys.* **7**, 1103–1112 (1939).
35. L. Berthier, P. Charbonneau, A. Ninarello, M. Ozawa, S. Yaida, Zero-temperature glass transition in two dimensions. *Nat. Commun.* **10**, 1–7 (2019).
36. C. Scalliet, B. Guiselin, L. Berthier, Thirty milliseconds in the life of a supercooled liquid. *Phys. Rev. X* **12**, 041028 (2022).
37. W. W. Mullins, Thermodynamic equilibrium of a crystalline sphere in a fluid. *J. Chem. Phys.* **81**, 1436–1442 (1984).
38. P. Montero *et al.*, The young-Laplace equation for a solid-liquid interface. *J. Chem. Phys.* **153**, 191102 (2020).
39. K. Dawson *et al.*, Molecular packing in highly stable glasses of vapor-deposited tris-naphthylbenzene isomers. *J. Chem. Phys.* **136**, 094505 (2012).
40. V. Testard, L. Berthier, W. Kob, Influence of the glass transition on the liquid-gas spinodal decomposition. *Phys. Rev. Lett.* **106**, 125702 (2011).
41. V. Testard, L. Berthier, W. Kob, Intermittent dynamics and logarithmic domain growth during the spinodal decomposition of a glass-forming liquid. *J. Chem. Phys.* **140**, 164502 (2014).
42. T. M. Murphy, B. Freeman, D. Paul, Physical aging of polystyrene films tracked by gas permeability. *Polymer* **54**, 873–880 (2013).
43. R. R. Baglay, C. B. Roth, Communication: Experimentally determined profile of local glass transition temperature across a glassy-rubbery polymer interface with a T_g difference of 80 K. *J. Chem. Phys.* **143**, 111101 (2015).
44. L. Zheng, Q. An, Y. Xie, Z. Sun, S. N. Luo, Homogeneous nucleation and growth of melt in copper. *J. Chem. Phys.* **127**, 164503. (2007).
45. A. Samanta, M. E. Tuckerman, T. Q. Yu, W. E, Microscopic mechanisms of equilibrium melting of a solid. *Science* **346**, 729–732 (2014).
46. M. Ruiz-Ruiz, *et al.*, Real-time microscopic view of the relaxation of a glass. arXiv [Preprint] (2023). <http://arxiv.org/abs/2301.08458> (Accessed 20 January 2023).
47. B. Illing *et al.*, Mermin–Wagner fluctuations in 2D amorphous solids. *Proc. Natl. Acad. Sci. U.S.A.* **114**, 1856–1861 (2017).